

Canards in a Surface Oxidation Reaction

J. Moehlis

Program in Applied and Computational Mathematics, Princeton University, Princeton, NJ
08544-1000, USA
e-mail: jmoehlis@math.princeton.edu

Received May 10, 2001; revised January 24, 2002; accepted April 17, 2002
Online publication June 10, 2002
Communicated by Y. G. Kevrekidis

Summary. Canards are periodic orbits for which the trajectory follows both the attracting and repelling parts of a slow manifold. They are associated with a dramatic change in the amplitude and period of a periodic orbit within a very narrow interval of a control parameter. It is shown numerically that canards occur in an appropriate parameter range in two- and three-dimensional models of the platinum-catalyzed oxidation of carbon monoxide. By smoothly connecting associated stable and unstable manifolds in an asymptotic limit, we predict parameter values at which such canards exist. The relationship between the canards and saddle-loop bifurcations for these models is also demonstrated. Excellent agreement is found between the numerical and analytical results.

Key words. canards, slow manifold, singular perturbation, surface oxidation reaction

1. Introduction

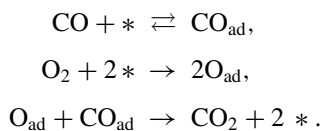
Canards are periodic orbits for which the trajectory follows both the *attracting* and *repelling* parts of a slow manifold. They are associated with a dramatic change in the amplitude and period of a periodic orbit within a very narrow interval of a control parameter. Canards may be present in singularly perturbed systems of ordinary differential equations (ODEs): A common scenario in which they arise is that a “small” stable periodic orbit is born in a supercritical Hopf bifurcation and rapidly changes to a “large” relaxation oscillation periodic orbit as a control parameter is varied. Canards are the intermediate periodic orbits between the small and large orbits—the shape of these periodic orbits in phase space can resemble a duck, hence the name “canard,” the French word for “duck.” Canards were first found in a study of the van der Pol system using techniques from nonstandard analysis [1], [2]; other useful references for this approach include [3], [4]. Responding to a challenge posed by nonstandard analysts, Eckhaus applied classical

asymptotic analysis to the study of canards [5] (see also [6], [7]). Later, an interpretation of canards in terms of invariant manifolds was given in [8]–[10]; a related approach is the use of geometric singular perturbation theory [11], [12], [13]. Canards also arise in the study of the singular Hopf bifurcation [14]–[16]. In addition to the van der Pol system (e.g. [2], [5], [17], [11], [18]), canards have been found and analyzed to varying degrees for a variety of chemical [10], [19]–[24], biological [14], [15], [25]–[28], and other systems [29]–[33]. For chemical systems (such as the system to be considered in this paper), canards may be important for diffusion-induced instabilities [34] and the presence of mixed-mode oscillations [23]. While much of the study of canards has been for two-dimensional systems, progress has also been made for higher-dimensional generalizations (e.g. [23], [28], [35], [36]). Issues related to the numerical computation of canards are discussed, for example, in [28], [37].

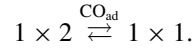
In this paper, canards are found and analyzed for models of the oxidation of carbon monoxide (CO) on the surface of platinum (Pt), where Pt serves as a catalyzing agent for the reaction. For simplicity, we ignore surface diffusion and assume that the system is isothermal. Section 2 discusses the model proposed by [38] for this system (a three-dimensional system of ODEs) and presents numerical evidence for the presence of canards. Canards have historically been considered for two-dimensional systems of equations (which also allows for a simpler interpretation), so Section 3 uses numerical arguments to justify a reduction to a two-dimensional model characterized by evolution of one variable on a fast timescale and the other on a slow timescale (cf. [39]). It is shown numerically that canards also exist for this two-dimensional model. Section 4 then gives an asymptotic analysis of the two-dimensional model in the spirit of [10]. Specifically, by smoothly connecting associated stable and unstable manifolds in an asymptotic limit, parameter values at which canards exist are predicted. Section 5 then extends the techniques used in Section 4 to predict parameter values at which canards exist for the full three-dimensional model. This procedure gives excellent agreement with results from numerical computations for both the two-dimensional and three-dimensional models, as described in Section 6. Section 7 then describes the relationship between canards and saddle-loop bifurcations for the models. Finally, Section 8 gives concluding remarks.

2. The Full Model

Oscillations in the oxidation of CO have been observed on surfaces of Pt defined by several different crystal planes (see, e.g., [40] and references therein). We focus on the Pt(110) surface for which oscillations have been found for temperatures T in the range $440K < T < 590K$ and partial pressures p_{CO} and p_{O_2} of CO and O_2 , respectively, in the range from 10^{-5} to 10^{-3} mbar, with $1 < p_{O_2}/p_{CO} < 24$ [40]. Chemically, oxidation proceeds via the Langmuir-Hinshelwood (LH) mechanism in which both CO and O_2 have to adsorb onto the catalytic Pt surface before reacting with each other [41]:



Here * denotes an empty adsorption site, and the subscript “ad” denotes an adsorbed species. Note that adsorbed CO inhibits the adsorption of oxygen, but the CO adsorption is not affected by adsorbed oxygen [42]. In addition, there is a dynamically occurring surface phase transition based on the CO coverage which is crucial to the presence of oscillations [38]:



The clean Pt(110) surface exhibits a 1×2 missing row structure, while the CO-covered surface exhibits a 1×1 structure. The fraction of the surface exhibiting the 1×1 structure between these extreme coverages increases monotonically with the CO coverage.

A three-dimensional system of ODEs for the isothermal Pt(110)-catalyzed oxidation of CO in the absence of surface diffusion was proposed in [38]:

$$\frac{du}{dt} = p_{\text{CO}} \kappa_c s_c \left(1 - \left(\frac{u}{u_s} \right)^3 \right) - k_d u - k_r u v, \quad (1)$$

$$\frac{dv}{dt} = p_{\text{O}_2} \kappa_o s_o \left(1 - \frac{u}{u_s} - \frac{v}{v_s} \right)^2 - k_r u v \equiv F_v(u, v, w), \quad (2)$$

$$\frac{dw}{dt} = k_p (h(u) - w). \quad (3)$$

Here u is the surface coverage of CO, v is the surface coverage of oxygen, and w is the fraction of the surface area exhibiting the 1×1 structure. The variables u, v, w must each lie in the interval $[0, 1]$. The sticking coefficient of oxygen depends on the surface structure and is given by

$$s_o = w s_{o1} + (1 - w) s_{o2}. \quad (4)$$

The function $h(u)$ is found by fitting experimental data, and in [38] was taken to be the C^1 function

$$h(u) \equiv \begin{cases} 0 & u \leq 0.2 \\ \sum_{i=0}^3 r_i u^i & 0.2 \leq u \leq 0.5, \\ 1 & u > 0.5 \end{cases}$$

where

$$r_3 = -\frac{1}{0.0135}, \quad r_2 = -1.05r_3, \quad r_1 = 0.3r_3, \quad r_0 = -0.026r_3.$$

Note that $h''(u)$ is discontinuous at $u = 0.2$ and $u = 0.5$. The reaction rates k_r, k_d, k_p are found from the Arrhenius law:

$$k_i = k_i^0 \exp \left[-\frac{E_i}{RT} \right], \quad i = r, d, p.$$

Following [38], the physical constants will be taken to be the values given in Table 1.

For the physical parameters of interest, the model given by (1–3) always has at least one and may have up to three fixed points. In addition, the model can have periodi-

Table 1. Physical constants for the model given by (1–3), following [38].

CO adsorption	Rate of CO hitting surface	$\kappa_c = 3.135 \times 10^5 \text{ s}^{-1} \text{ mbar}^{-1}$
	Sticking coefficient	$s_c = 1$
	Saturation coverage	$u_s = 1$
O ₂ adsorption	Rate of O hitting surface	$\kappa_o = 5.858 \times 10^5 \text{ s}^{-1} \text{ mbar}^{-1}$
	Sticking coefficients	$s_{o1} = 0.6, s_{o2} = 0.4$
	Saturation coverage	$v_s = 0.8$
Rates	Reaction	$k_r^0 = 3 \times 10^6 \text{ s}^{-1}$ $E_r = 10 \text{ kcal/mol}$
	Desorption of CO	$k_d^0 = 2 \times 10^{16} \text{ s}^{-1}$ $E_d = 38 \text{ kcal/mol}$
	Phase transition	$k_p^0 = 1 \times 10^2 \text{ s}^{-1}$ $E_p = 7 \text{ kcal/mol}$
	Gas constant	$R = 0.001987 \text{ kcal/(K mol)}$

cally oscillating solutions according to the following mechanism. Suppose that we start with small CO coverage (i.e., u is small), which implies that the fraction of the surface with the 1×1 structure will be small (i.e., w is small). Furthermore, suppose that the partial pressures have been chosen so that, taking into account the fact that adsorbed CO inhibits the adsorption of oxygen, the adsorption of CO dominates (i.e., u is increasing and v is decreasing). The increasing coverage of CO increases the fraction of the surface with the 1×1 structure (i.e., w increases), thereby increasing the sticking coefficient s_o for oxygen. The resulting increased oxygen coverage leads to increased reaction between CO_{ad} and O_{ad} to give CO_2 , which decreases the CO coverage (i.e., u decreases). The decreasing CO coverage causes the fraction of the surface with the 1×1 structure to decrease (i.e., w decreases). This lowers s_o , so that the coverage of oxygen decreases (i.e., v decreases). Thus, we are back where we started: u and w are small, and the adsorption of CO will dominate. The process then starts over again, giving oscillations.

Bifurcation sets for fixed point and periodic solutions of (1–3) are discussed in detail in [38]. Figure 1 shows representative results for $T = 540\text{K}$; these were obtained using the numerical continuation package AUTO [43] and reproduce the results of Figure 8 of [38]. We motivate our upcoming analysis by considering the bifurcation diagram corresponding to a slice through parameter space for fixed $T = 540\text{K}$, fixed $p_{\text{CO}} = 45 \times 10^{-6} \text{ mbar}$, and varying p_{O_2} (see Figure 2(a)). For decreasing p_{O_2} , a periodic orbit is born in a supercritical Hopf bifurcation at

$$p_{\text{O}_2}^{\text{h,3D}} = 148.1002 \times 10^{-6} \text{ mbar}, \quad (5)$$

and dies when a saddle-node bifurcation of fixed points occurs on it at $p_{\text{O}_2} = 138.9732 \times 10^{-6} \text{ mbar}$. Although the periodic orbit deforms smoothly as p_{O_2} is varied over this range, there is clearly a small range of parameters over which it very rapidly changes its characteristics (see the inset of Figure 2(a) and the time series plots in Figure 2(b,c)). Careful numerics using a variable-step fourth-order Runge-Kutta scheme with a maximum step size of 0.01 show that this transition occurs at

$$p_{\text{O}_2}^{\text{c,3D}} \approx 147.741139211546 \times 10^{-6} \text{ mbar}. \quad (6)$$

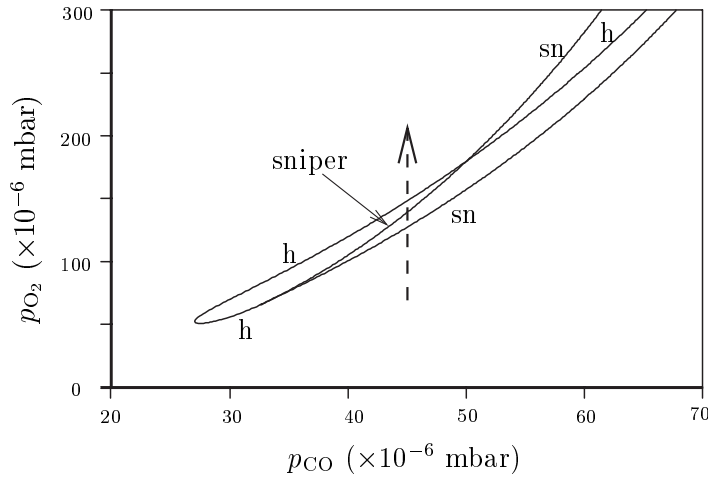


Fig. 1. Bifurcation sets for $T = 540K$. The lines labeled h, sn, and sniper correspond to Hopf bifurcations, saddle-node bifurcations of fixed points, and saddlenode bifurcations of fixed points occurring on the periodic orbit, respectively. The dashed vertical line shows the cut through parameter space giving the results shown in Figure 2(a).

This parameter value is given to such high accuracy because larger values (even increasing the last decimal to 7) give a “small” periodic orbit as in Figure 2(b), while smaller values (even decreasing the last decimal to 5) give a “large” periodic orbit as in Figure 2(c). The periodic orbits for p_{O_2} near $p_{O_2}^{c,3D}$ are canards. The “large” relaxation oscillation limit cycles could be approximated using matched asymptotic expansions as described, e.g., in [44]. However, in this paper we focus on the canards: By applying asymptotic analysis to a reduced model of (1–3) and then to the full equations, we will show how to predict with very high accuracy parameter values at which such transitions occur, and hence parameter values near which canards will be present.

Before proceeding, we note that not all cuts through parameter space will give a rapid change in the characteristics of the periodic orbit such as we saw in Figure 2. Figure 3 shows the bifurcation diagram corresponding to fixed $T = 540K$, fixed $p_{CO} = 30 \times 10^{-6} \text{ mbar}$, and varying p_{O_2} . A periodic orbit is born and dies in supercritical Hopf bifurcations at $p_{O_2} = 55.8552 \times 10^{-6} \text{ mbar}$ and $p_{O_2} = 69.8219 \times 10^{-6} \text{ mbar}$, and shows no sudden change in characteristics over the parameter range for which it exists.

For reference, we also note the presence of codimension-two bifurcations for (1–3) as given in Table 2 for $T = 540K$; these bifurcations are discussed in [38] (see, e.g., Figure 9 of that paper). The neutral-saddle-loop bifurcation is not resolved because of the difficulty in reliably detecting saddle-node bifurcations of periodic orbits near parameter values at which canards exist. Here we remark only that several of these codimension-two bifurcations have associated codimension-one saddle-loop bifurcations [45], [38]; the relationship of these saddle-loop bifurcations to canards will be discussed in Section 7.

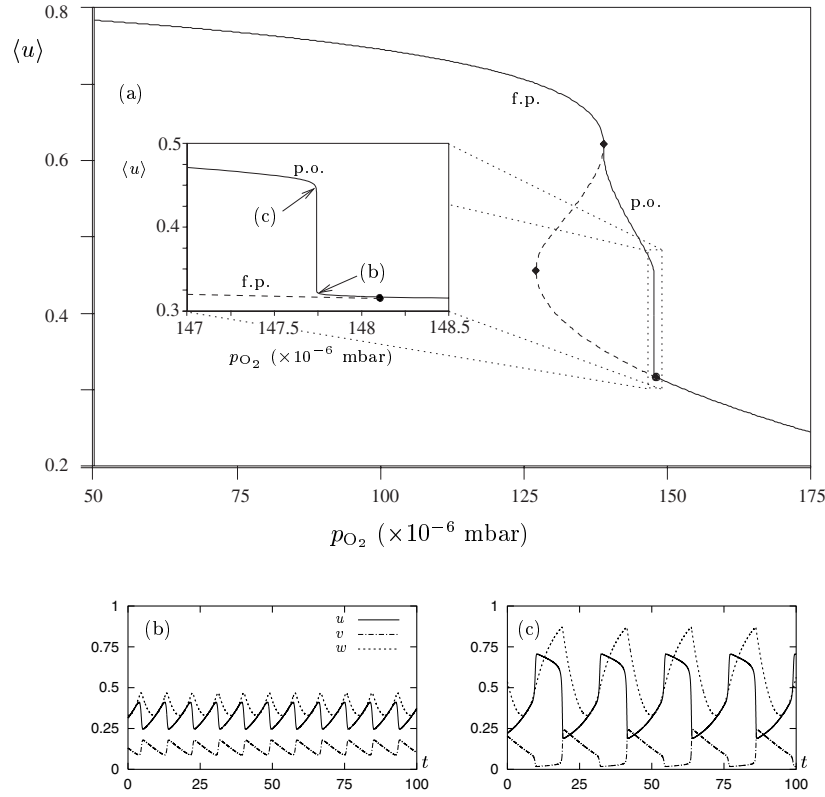


Fig. 2. (a) Bifurcation diagram for fixed $T = 540\text{K}$ and fixed $p_{\text{CO}} = 45 \times 10^{-6}$ mbar corresponding to the dashed vertical line in Figure 1. $\langle u \rangle$ is the time-average of u for the solution. The branches labeled f.p. (p.o.) are fixed point (periodic orbit) branches. Solid (dashed) lines indicate stable (unstable) solutions. Circles (diamonds) indicate Hopf (saddle-node) bifurcations. The inset zooms in on the parameter range for which the periodic orbit rapidly changes its characteristics. The time series for stable periodic orbits on both sides of this transition are shown for (b) $p_{\text{O}_2} = 147.742 \times 10^{-6}$ mbar and (c) $p_{\text{O}_2} = 147.740 \times 10^{-6}$ mbar.

Table 2. Codimension-two bifurcations for (1–3) for $T = 540\text{K}$ using the notation of [38].

Bifurcation	$p_{\text{CO}} (\times 10^{-6} \text{ mbar})$	$p_{\text{O}_2} (\times 10^{-6} \text{ mbar})$
Takens-Bogdanov	32.8	66.3
Takens-Bogdanov	114.9	1289.7
Cusp	32.6	65.4
Cusp	167.7	6823.0
Saddle-node loop	33	67
Saddle-node loop	50	180
Degenerate Hopf	62	271
Neutral-saddle loop	unresolved	unresolved

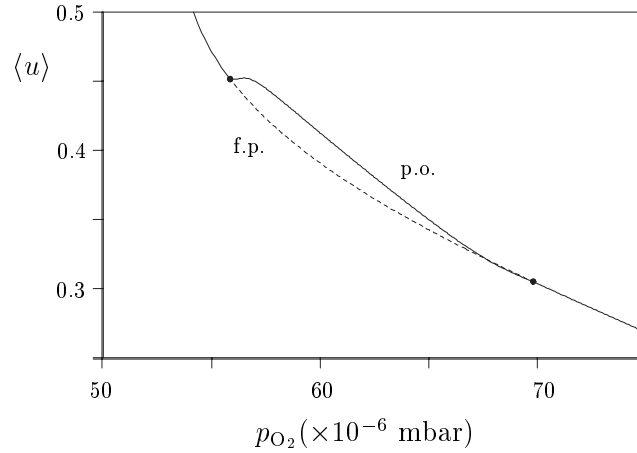


Fig. 3. Bifurcation diagram for fixed $T = 540K$ and fixed $p_{CO} = 30 \times 10^{-6}$ mbar with the same conventions as in Figure 2(a).

3. Reduction to a Two-Dimensional Model

Numerical integration of (1–3) suggests that the variable v can be replaced by its adiabatic value, i.e., the value obtained by solving $F_v(u, v, w) = 0$ for v [39]. This is not obvious from the examination of the smallness of different parameters [39], and before giving the resulting equations we examine the validity of the approximation in more detail. Our discussion is for a specific set of parameter values; similar results are found throughout the parameter range of interest.

Consider the parameters $T = 540K$, $p_{CO} = 45 \times 10^{-6}$ mbar, and $p_{O_2} = 147.740 \times 10^{-6}$ mbar; the stable periodic orbit for these parameters was shown in Figure 2(c). For these parameter values there is also an unstable fixed point at $(u, v, w) = (0.317875, 0.128795, 0.341832)$ with eigenvalues

$$\lambda_s = -185.735, \quad \rho_u \pm i\omega_u = 0.0375 \pm 1.2174i. \quad (7)$$

The large negative eigenvalue causes trajectories in the neighborhood of the fixed point to rapidly approach a two-dimensional surface which can be approximated locally by doing an unstable manifold reduction (this is completely analogous to a center manifold reduction as described, e.g., in [45]). The resulting two-dimensional surface, approximated to quadratic order and found with the assistance of Mathematica, is shown in Figure 4; also shown is the two-dimensional surface defined by $F_v(u, v, w) = 0$ and the trajectory on the stable periodic orbit. The two surfaces are nearly coincident, which provides strong evidence that near the fixed point the adiabatic approximation for v is very good.

The validity of the adiabatic approximation away from the fixed point is explored by numerically calculating the distance from the trajectory on a periodic orbit to the surface defined by $F_v(u, v, w) = 0$. Specifically, this distance is found by minimizing

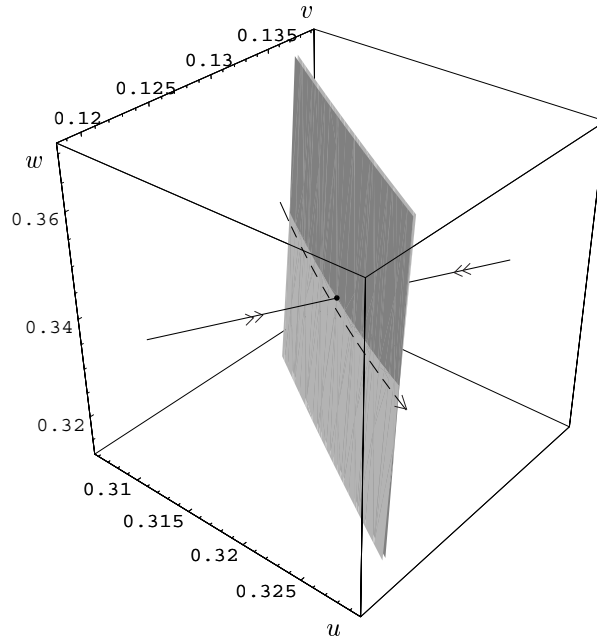


Fig. 4. Results for the parameters $T = 540K$, $p_{CO} = 45 \times 10^{-6}$ mbar, and $p_{O_2} = 147.740 \times 10^{-6}$ mbar. The (unstable) fixed point is shown as a solid dot. The lines with double arrows are the strongly contracting directions defined by the eigenvector for the negative eigenvalue of the fixed point. The darker (lighter) surface shows the local quadratic approximation to the unstable manifold of the fixed point (the surface defined by $F_v(u, v, w) = 0$); the intersection of these surfaces is a curve passing through the fixed point. The dashed line shows a segment of the trajectory on the (stable) periodic orbit which lies very near the unstable manifold. Clearly, near the fixed point the adiabatic approximation for v is excellent.

the quantity

$$d = [(u_{po}(t) - u)^2 + (v_{po}(t) - v)^2 + (w_{po}(t) - w)^2]^{1/2}, \quad (8)$$

for each t subject to the constraint $F_v(u, v, w) = 0$, where $(u_{po}(t), v_{po}(t), w_{po}(t))$ is the position on the periodic orbit at time t . This leads to the algebraic system of equations

$$\begin{aligned} \frac{\partial d}{\partial u} &= \lambda \frac{\partial F_v}{\partial u}, & \frac{\partial d}{\partial v} &= \lambda \frac{\partial F_v}{\partial v}, \\ \frac{\partial d}{\partial w} &= \lambda \frac{\partial F_v}{\partial w}, & F_v(u, v, w) &= 0, \end{aligned}$$

to be solved for u, v, w, λ for each t (here λ is a Lagrange multiplier). The values obtained for u, v, w then allow the computation of d as a function of t using (8). Figure 5 shows

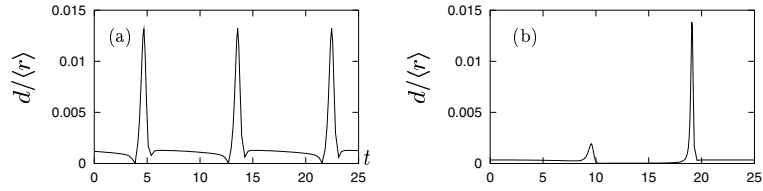


Fig. 5. Normalized distance $d/\langle r \rangle$ between the trajectory on the stable periodic orbit and the surface defined by $F_v(u, v, w) = 0$ for $T = 540K$, $p_{O_2} = 45 \times 10^{-6}$, and (a) $p_{O_2} = 147.742 \times 10^{-6}$ mbar and (b) $p_{O_2} = 147.740 \times 10^{-6}$ mbar. The initial conditions are the same as for the corresponding plots in Figure 2(b,c), but the time axis has a different scale.

$d/\langle r \rangle$ for the periodic orbits shown in Figure 2(b,c), where

$$\langle r \rangle \equiv \langle [(u_{po}(t) - \langle u \rangle)^2 + (v_{po}(t) - \langle v \rangle)^2 + (w_{po}(t) - \langle w \rangle)^2]^{1/2} \rangle,$$

and $\langle \cdot \rangle$ denotes the time-average. $\langle r \rangle$ is thus the ‘‘average radius’’ of the periodic orbit, and is approximately 0.0719 and 0.2731 for the cases shown in Figure 5(a) and (b), respectively. There are spikes during fast phases of the motion, but in both cases $d/\langle r \rangle$ remains quite small throughout the entire periodic orbit. Indeed, the maximum value of $d/\langle r \rangle$ is approximately 0.015 for both periodic orbits. Similar results hold for other parameter values, so we conclude that the approximation made in [39] that v can be replaced by its adiabatic value is quite good, even away from the fixed point.

Letting $t' = k_p t$ and dropping the prime, (1–3) may be rewritten as

$$\epsilon \frac{du}{dt} = \beta(1 - u^3) - \gamma u - uv/v_s \equiv f_u(u, v), \quad (9)$$

$$\epsilon \frac{dv}{dt} = \alpha(w + s)(1 - u - v/v_s)^2 - uv/v_s \equiv f_v(u, v, w; \alpha), \quad (10)$$

$$\frac{dw}{dt} = h(u) - w \equiv g(u, w), \quad (11)$$

where

$$\alpha = \frac{p_{O_2} \kappa_o (s_{o1} - s_{o2})}{k_r v_s}, \quad \beta = \frac{p_{CO} \kappa_c}{k_r v_s}, \quad \gamma = \frac{k_d}{k_r v_s},$$

$$\epsilon = \frac{k_p}{k_r v_s}, \quad s = \frac{s_{o2}}{s_{o1} - s_{o2}} = 2,$$

and we have used the fact that $s_c = u_s = 1$. The quantities α , β , γ , ϵ , and s are dimensionless. Solving $f_v(u, v, w; \alpha) = 0$ for v (i.e., making the adiabatic approximation), we obtain (cf. [39])

$$v = v_s y(u, w),$$

where

$$y(u, w) \equiv 1 - u + Au - \sqrt{2Au(1 - u) + (Au)^2}, \quad A \equiv \frac{1}{2\alpha(w + s)}. \quad (12)$$

This gives the two-dimensional model

$$\epsilon \frac{du}{dt} = f(u, w), \quad (13)$$

$$\frac{dw}{dt} = g(u, w), \quad (14)$$

where

$$f(u, w) \equiv \beta(1 - u^3) - \gamma u - uy(u, w). \quad (15)$$

Note that the expression for γ in [39] has a typo, in that u_s should be replaced by v_s .

Figure 6 shows numerically calculated stable periodic orbits for (13,14) for $T = 540K$, $p_{CO} = 45 \times 10^{-6}$ mbar, and with different values of p_{O_2} . These results were obtained using a variable-step fourth-order Runge-Kutta scheme with a maximum step size of 0.01. Note the very rapid change in the shape of the periodic orbit as p_{O_2} is varied by only a tiny amount. Numerically, the transition between “small” and “large” periodic orbits occurs at

$$p_{O_2}^{c,2D} \approx 147.9057052043 \times 10^{-6} \text{ mbar}. \quad (16)$$

Canards are the periodic orbits which are present very close to this parameter value and which follow the $\frac{dw}{dt} = 0$ nullcline for an appreciable distance after crossing the $\frac{du}{dt} = 0$ nullcline. For reference, the Hopf bifurcation for (13,14) for these parameters occurs at

$$p_{O_2}^{h,2D} = 148.2408 \times 10^{-6} \text{ mbar}. \quad (17)$$

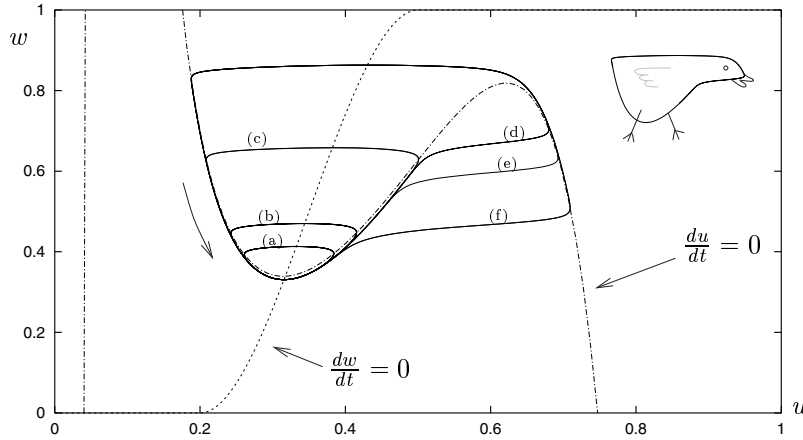


Fig. 6. Stable periodic orbits for (13,14) with $T = 540K$, $p_{CO} = 45 \times 10^{-6}$ mbar, and (a) $p_{O_2} = 147.91 \times 10^{-6}$ mbar, (b) $p_{O_2} = 147.90575 \times 10^{-6}$ mbar, (c) $p_{O_2} = 147.90570520432 \times 10^{-6}$ mbar, (d) $p_{O_2} = 147.90570520431 \times 10^{-6}$ mbar, (e) $p_{O_2} = 147.9057052 \times 10^{-6}$ mbar, (f) $p_{O_2} = 147.905 \times 10^{-6}$ mbar. The dashed line is the nullcline of $g(u, w)$, while the dash-dotted line is the nullcline of $f(u, w)$ (the nullclines do not change appreciably over the range of p_{O_2} shown in the figure). The sketch in the corner shows why the name “canard” was introduced to describe such solutions. Solutions such as (c) and (d) are sometimes referred to as “a duck without a head” and “a duck with a head,” respectively.

The closeness of $p_{\text{O}_2}^{\text{h},2\text{D}}$ to $p_{\text{O}_2}^{\text{h},3\text{D}}$ (comparing (17) to (5)) and $p_{\text{O}_2}^{\text{c},2\text{D}}$ to $p_{\text{O}_2}^{\text{c},3\text{D}}$ (comparing (16) to (6)) provides further evidence of the validity of the adiabatic approximation for v .

In the next section, we will show how to predict the parameter value $p_{\text{O}_2}^{\text{c}}$ at which the transition between “small” and “large” periodic orbits occurs. For a typical operating temperature $T \approx 540\text{K}$, we find that $\epsilon \approx 1 \times 10^{-3} \ll 1$. We are thus led to study (13,14) as singularly perturbed differential equations. We note from (7) that $|\rho_u/\lambda_s| \approx 2 \times 10^{-4} \ll \epsilon$, that is, even though ϵ is small, it is not as small as the ratio of the real parts of the slow and fast eigenvalues for the three-dimensional system. Thus, reduction from a three-dimensional system to a two-dimensional system followed by singular asymptotics on the reduced system seems justified. It will be useful to introduce a new time variable $\tau = t/\epsilon$ which takes (13,14) into

$$\frac{du}{d\tau} = f(u, w), \quad (18)$$

$$\frac{dw}{d\tau} = \epsilon g(u, w). \quad (19)$$

4. Asymptotic Analysis of the Canard Manifold for the Two-Dimensional Model

From (12) and (15), the nullcline $S = \{(u, w) \mid f(u, w) = 0\}$ is given by

$$w = -\frac{u^2(\gamma u + \beta(u^3 - 1)) + \alpha s((1 + \gamma - u)u + \beta(u^3 - 1))^2}{\alpha((1 + \gamma - u)u + \beta(u^3 - 1))^2}. \quad (20)$$

If ϵ is (artificially) taken to be zero, (18,19) imply that S is invariant and consists entirely of fixed points. Also, trajectories in phase space will obey $\frac{dw}{du} = 0$. Figure 7 shows S and the corresponding trajectories for $\epsilon = 0$ and $T = 540\text{K}$, $p_{\text{CO}} = 45 \times 10^{-6}$ mbar, $p_{\text{O}_2} = 148 \times 10^{-6}$ mbar, i.e., with

$$\alpha = 0.0806091, \quad \beta = 0.0655833, \quad \gamma = 0.0386961. \quad (21)$$

It also shows the points M and N which are defined as the local minima and maxima of the graph of S , respectively. The direction of the trajectories follows from the fact that $f(u, w) < 0 (> 0)$ for points in (u, w) space above (below) S , as may be readily verified. Alternatively, for $\epsilon = 0$ the Jacobian for the fixed points on S from (18,19) is

$$J = \begin{pmatrix} \left. \frac{\partial f}{\partial u} \right|_S & \left. \frac{\partial f}{\partial w} \right|_S \\ 0 & 0 \end{pmatrix}.$$

Thus, each fixed point has one zero eigenvalue, and one eigenvalue equal to $(\partial f/\partial u)|_S$. With Mathematica, we calculate the nontrivial eigenvalue for these parameters (see Figure 8). This nontrivial eigenvalue is negative (positive) for the pieces of S which are attracting (repelling). It is equal to zero only at the points M and N .

The curve S is said to be *normally hyperbolic* on the pieces for which $(\partial f/\partial u)|_S$ is bounded away from zero. Invariant manifold theorems then imply that for ϵ sufficiently

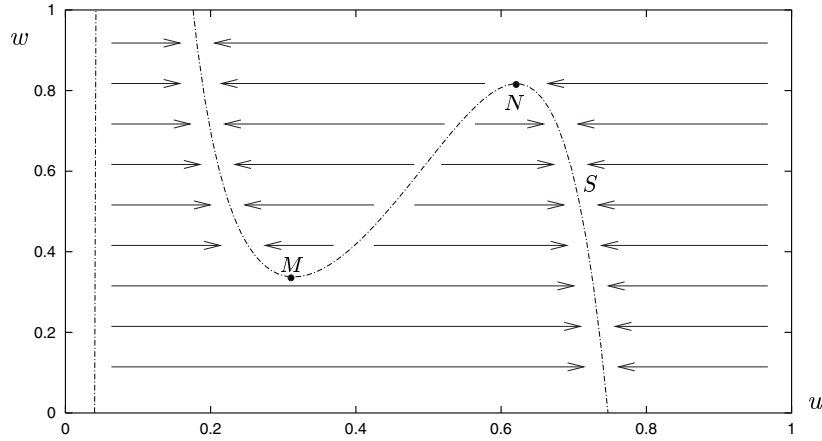


Fig. 7. The curve S and phase space trajectories for $T = 540K$, $p_{\text{CO}} = 45 \times 10^{-6}$ mbar, and $p_{\text{O}_2} = 148 \times 10^{-6}$ mbar but with ϵ artificially taken to be zero.

small, invariant manifolds persist within $\mathcal{O}(\epsilon)$ of these pieces; these manifolds inherit their normal stability properties from the original pieces of S [46], [47], [48]. Specifically, there will be a stable (unstable) manifold M_S (M_U) within $\mathcal{O}(\epsilon)$ of the attracting (repelling) pieces of S . Both M_S and M_U can be extended beyond the points M and N according to the flow, but the extensions may leave an $\mathcal{O}(\epsilon)$ distance of S and may also lose their normal stability properties. Generically, the distance between M_S and M_U is nonzero near M and N . The two generic situations near M for $\epsilon > 0$ are shown in Figure 9 (cf. Figure 2 of [10] and Figures 9 and 10 of [13]). Consider a trajectory which follows the stable manifold M_S . For the case shown in Figure 9(a), near M the trajectory

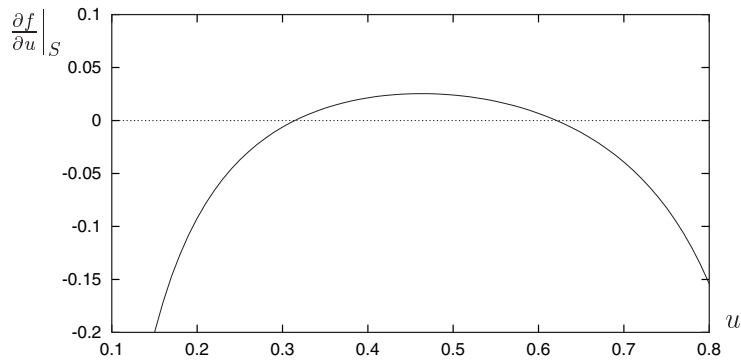


Fig. 8. The nontrivial eigenvalue $\frac{\partial f}{\partial u}|_S$ as a function of u for $T = 540K$, $p_{\text{CO}} = 45 \times 10^{-6}$ mbar, and $p_{\text{O}_2} = 148 \times 10^{-6}$ mbar but with ϵ artificially taken to be zero.

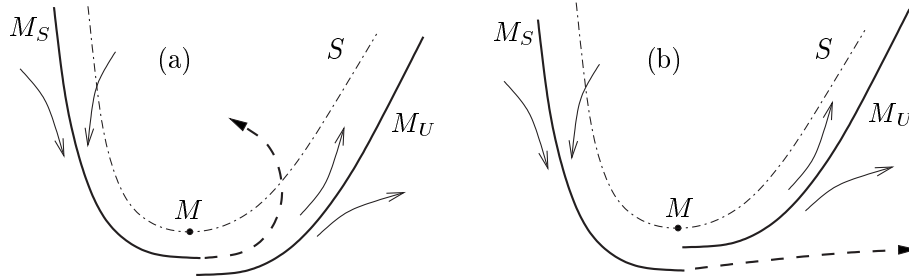


Fig. 9. The two generic situations for the relative positions of the stable and unstable manifolds near M for $\epsilon > 0$. The trajectory follows the stable manifold M_S , and after passing near M may either (a) cross S and return quickly to a neighborhood of M_S , or (b) undergo a large excursion before returning to a neighborhood of M_S .

is pushed to the left, crosses S , and quickly returns to the vicinity of M_S . On the other hand, for the case shown in Figure 9(b), near M the trajectory is pushed to the right, and can only return to the vicinity of M_S after a large excursion through another part of phase space. The distance between M_S and M_U near M changes as parameters are varied, and it is possible for particular parameters that the manifolds M_S and M_U will connect smoothly. Following [10], the invariant curve is then called the *canard manifold*. In this situation, the trajectory follows the canard manifold both along its attracting and repelling parts. (See [12] and [13] for a more detailed discussion of the relationship between canards and invariant manifolds.)

The canard manifold lacks normal hyperbolicity at the point where M_S connects with M_U and may therefore be nonunique. As an illustration of this point, consider the vector field

$$\frac{dX}{dt} = \epsilon(\mu + X^2), \quad \frac{dY}{dt} = XY, \tag{22}$$

for $0 < \mu < 1$ and $\epsilon \ll 1$. For $\epsilon = 0$, $S \equiv \{(X, Y) \mid Y = 0\}$ defines a curve of fixed points. A linear stability analysis shows that for any $\delta > 0$, the set $S_- \equiv \{(X, Y) \mid Y = 0, X < -\delta\}$ is normally attracting and the set $S_+ \equiv \{(X, Y) \mid Y = 0, X > \delta\}$ is normally repelling. As described above, for ϵ sufficiently small, invariant manifolds M_S and M_U persist within $\mathcal{O}(\epsilon)$ of S_- and S_+ , respectively. A canard manifold is obtained by smoothly connecting M_S and M_U . Now, t may be eliminated as an independent variable from (22) to give

$$\frac{dY}{dX} = \frac{XY}{\epsilon(\mu + X^2)}.$$

This has solutions

$$Y(X) = c(X^2 + \mu)^{1/(2\epsilon)} \tag{23}$$

for any c . As $\epsilon \rightarrow 0$, $Y(X)$ and all of its derivatives are equal to zero at $X = 0$. Thus, (23) gives a one-parameter family of manifolds (parametrized by c) which smoothly connect

M_S and M_U in the limit $\epsilon \rightarrow 0$. Each of these manifolds is a canard manifold. Fortunately, this nonuniqueness of canard manifolds will not affect our asymptotic analysis later in this section because we only impose conditions in a very small neighborhood of where M_S and M_U smoothly connect (cf. the results for the nonuniqueness of the center manifold in [49]; see also [13]).

In a typical scenario for the oxidation models considered in this paper, a “small” stable periodic orbit is born in a supercritical Hopf bifurcation, with the manifolds as sketched in Figure 9(a). As the control parameter is varied away from the Hopf bifurcation point, the relative position of the manifolds switches to the case sketched in Figure 9(b), giving a “large” stable periodic orbit. The canards are the intermediate periodic orbits between the small and large periodic orbits, and are expected to exist for a range of control parameters of $\mathcal{O}(e^{-K/\epsilon})$ for some $K > 0$ as $\epsilon \rightarrow 0$ [5], [13].

In the remainder of this section, we will find equations for the parameter values at which canard solutions exist for the oxidation model by requiring the existence of a canard manifold which stays within $\mathcal{O}(\epsilon)$ of S . This is accomplished through asymptotic expansions, and we closely follow the procedure given in [10]. Similar calculations have also been done from the perspective of nonstandard analysis (e.g. [4]). Note that for the simpler case of the van der Pol equation, it has been proven that the corresponding asymptotic series obtained by this procedure has zero radius of convergence [50]. However, experience has shown that the first few terms often give very good results. Here we will only calculate the first two terms in the asymptotic series. In Section 6 we will compare the predictions of this section with numerical results for both the two- and three-dimensional models given by (13,14) and (9–11), respectively, and find astounding agreement!

For definiteness, we hold T and p_{CO} fixed and vary p_{O_2} . In other words, we are treating the parameters $\beta, \gamma, \epsilon, s$ as fixed, and allow only α to vary. We will derive equations for the first two terms in an asymptotic expansion for the value of α at which canard solutions exist. A similar procedure to that given below could be used to analyze cases where T or p_{CO} are allowed to vary. From (13,14), trajectories obey

$$[\beta(1 - u^3) - \gamma u - uy(u, w)] \frac{dw}{du} = \epsilon[h(u) - w]. \quad (24)$$

We expand α in powers of ϵ about a fixed value α_0 to be defined below:

$$\alpha = \alpha_0 + \epsilon\alpha_1 + \epsilon^2\alpha_2 + \dots \quad (25)$$

We seek an approximation to the canard manifold:

$$w(u; \alpha) = w_0(u; \alpha_0) + \epsilon w_1(u; \alpha_0, \alpha_1) + \epsilon^2 w_2(u; \alpha_0, \alpha_1, \alpha_2) + \dots \quad (26)$$

Finally, using (26) to express w in terms of u , we expand

$$y(u, w; \alpha) = y_0(u; \alpha_0) + \epsilon y_1(u; \alpha_0, \alpha_1) + \epsilon^2 y_2(u; \alpha_0, \alpha_1, \alpha_2) + \dots \quad (27)$$

For future reference, we obtain equations for y_0 and y_1 in terms of the w_i 's by expanding (12) in powers of ϵ :

$$\begin{aligned}
 y_0 &= 1 - u + \frac{u}{2\alpha_0(w_0 + s)} - \left(\frac{u(1-u)}{\alpha_0(w_0 + s)} + \left(\frac{u}{2\alpha_0(w_0 + s)} \right)^2 \right)^{1/2} \\
 &= \frac{u - 2\alpha_0(u-1)(w_0 + s) - \sqrt{u^2 - 4\alpha_0u(u-1)(w_0 + s)}}{2\alpha_0(w_0 + s)}, \tag{28}
 \end{aligned}$$

$$y_1 = \frac{u[\alpha_1(w_0 + s) + \alpha_0w_1]}{2\alpha_0^2(w_0 + s)^2} \left[\frac{u - 2\alpha_0(u-1)(w_0 + s)}{\sqrt{u^2 - 4\alpha_0u(u-1)(w_0 + s)}} - 1 \right], \tag{29}$$

where for brevity $w_0 = w_0(u; \alpha_0)$ and $w_1 = w_1(u; \alpha_0, \alpha_1)$. For the asymptotic expansions (25–27) to be valid, it is necessary that $w_i = \mathcal{O}(1)$ and $y_i = \mathcal{O}(1)$ for $i = 0, 1, \dots$

At $\mathcal{O}(\epsilon^0)$, (24) gives

$$[\beta(1 - u^3) - \gamma u - u y_0] \frac{dw_0}{du} = 0.$$

For a nontrivial w_0 ,

$$\beta(1 - u^3) - \gamma u - u y_0 = 0. \tag{30}$$

Using (28), this implies that

$$w_0(u; \alpha_0) = - \frac{u^2(\gamma u + \beta(u^3 - 1)) + \alpha_0s((1 + \gamma - u)u + \beta(u^3 - 1))^2}{\alpha_0((1 + \gamma - u)u + \beta(u^3 - 1))^2}. \tag{31}$$

Comparing this with (20), we see that $w_0(u; \alpha_0)$ describes the nullcline $f(u, w) = 0$ when $\alpha = \alpha_0$. This is as expected because the canard manifold is an $\mathcal{O}(\epsilon)$ distance from the slow manifold S which exists for $\epsilon = 0$. We define u_M to be the u coordinate at the local minimum M of the graph of $w_0(u; \alpha_0)$ (see Figure 7).

To define the quantity α_0 , we need to consider (24) at $\mathcal{O}(\epsilon)$. Using (30), we obtain

$$-u y_1 \frac{dw_0}{du} = h(u) - w_0(u; \alpha_0).$$

Rearranging,

$$y_1 = \frac{w_0(u; \alpha_0) - h(u)}{u w_0'(u; \alpha_0)}, \tag{32}$$

where the prime denotes differentiation with respect to u . Notice that by the definition of u_M , $w_0'(u; \alpha_0) \rightarrow 0$ as $u \rightarrow u_M$. In order to keep y_1 bounded (as required for the asymptotic expansion to be valid), it is necessary that

$$\lim_{u \rightarrow u_M} [w_0(u; \alpha_0) - h(u)] = w_0(u_M; \alpha_0) - h(u_M) = 0.$$

Thus, we choose α_0 so that $w_0(u_M; \alpha_0) = h(u_M)$. But from (14), this is the condition that $\frac{dw}{dt} = 0$ at $(u, w) = (u_M, w_0(u_M; \alpha_0))$; recalling that $w_0(u_M; \alpha_0)$ is the nullcline

where $\frac{du}{dt} = 0$ for $\alpha = \alpha_0$, we conclude that the value of α_0 is that for which a fixed point to (13,14) exists at point M . The values of α_0 and u_M are found by solving the simultaneous equations

$$w_0(u_M; \alpha_0) = h(u_M), \quad w_0'(u_M; \alpha_0) = 0. \quad (33)$$

Because of the complicated form of the functions, this is best done numerically for specific parameters.

In the following, we will need expressions for y_1 and y_1' in the limit as $u \rightarrow u_M$. These follow from applying L'Hôpital's rule to (32) and its derivative with respect to u :

$$\lim_{u \rightarrow u_M} y_1 = -\frac{h'(u_M)}{u_M w_0''(u_M; \alpha_0)}, \quad (34)$$

$$\begin{aligned} \lim_{u \rightarrow u_M} y_1' &= (-u_M h''(u_M) w_0''(u_M; \alpha_0) + u_M [w_0''(u_M; \alpha_0)]^2 \\ &\quad + h'(u_M) (2w_0''(u_M; \alpha_0) + u_M w_0'''(u_M; \alpha_0)) / (2u_M^2 [w_0''(u_M; \alpha_0)]^2). \end{aligned} \quad (35)$$

An equation for α_1 can now be obtained by considering (24) at $\mathcal{O}(\epsilon^2)$. Using (30),

$$-u y_1 \frac{dw_1}{du} - u y_2 \frac{dw_0}{du} = -w_1.$$

Rearranging,

$$y_2 = \frac{w_1(u; \alpha_0, \alpha_1) - u y_1 w_1'(u; \alpha_0, \alpha_1)}{u w_0'(u; \alpha_0)}.$$

Similar to above, since the denominator of this expression goes to zero as $u \rightarrow u_M$, in order to keep y_2 bounded it is necessary that

$$\lim_{u \rightarrow u_M} [w_1(u; \alpha_0, \alpha_1) - u y_1 w_1'(u; \alpha_0, \alpha_1)] = 0.$$

Using (34), this becomes

$$\lim_{u \rightarrow u_M} [w_1(u; \alpha_0, \alpha_1)] + \frac{h'(u_M)}{w_0''(u_M; \alpha_0)} \lim_{u \rightarrow u_M} [w_1'(u_M; \alpha_0, \alpha_1)] = 0. \quad (36)$$

Now, rearranging (29), we obtain

$$w_1(u; \alpha_0, \alpha_1) = G(u; \alpha_0) y_1 + H(u; \alpha_0, \alpha_1), \quad (37)$$

where

$$G(u; \alpha_0) = \frac{2\alpha_0(w_0 + s)^2}{u \left[\frac{u - 2\alpha_0(u-1)(w_0+s)}{\sqrt{u^2 - 4\alpha_0 u(u-1)(w_0+s)}} - 1 \right]}, \quad H(u; \alpha_0, \alpha_1) = -\frac{\alpha_1}{\alpha_0} (w_0 + s).$$

Therefore,

$$\begin{aligned} \lim_{u \rightarrow u_M} [w_1(u; \alpha_0, \alpha_1)] &= G(u_M; \alpha_0) \left(\lim_{u \rightarrow u_M} y_1 \right) + H(u_M; \alpha_0, \alpha_1), \\ \lim_{u \rightarrow u_M} [w_1'(u; \alpha_0, \alpha_1)] &= G'(u_M; \alpha_0) \left(\lim_{u \rightarrow u_M} y_1 \right) + G(u_M; \alpha_0) \left(\lim_{u \rightarrow u_M} y_1' \right) \\ &\quad + H'(u_M; \alpha_0, \alpha_1). \end{aligned}$$

With these expressions and using (34, 35), (36) becomes an equation for α_1 in terms of known quantities. We do not give an explicit expression for α_1 because it is quite cumbersome, but note that (36) can be solved numerically for specific parameters using, e.g., Mathematica.

In principle, we could continue this procedure to find $\alpha_2, \alpha_3, \dots$. However, as shown in Section 6, the calculations which we have given can already predict with excellent accuracy the parameter values for which canard solutions exist.

5. Asymptotic Analysis of the Canard Manifold for the Full Model

In this section, we show how the techniques of [10] as applied in Section 4 to the *two*-dimensional model can be extended to predict parameter values at which canards exist for the full *three*-dimensional model. As in Section 4, for definiteness we hold T and p_{CO} fixed and vary p_{O_2} ; a similar procedure to that given below could be used to analyze cases where T or p_{CO} are allowed to vary. Specifically, we consider equations (9–11) with $\tau = t/\epsilon$:

$$\frac{du}{d\tau} = f_u(u, v), \quad \frac{dv}{d\tau} = f_v(u, v, w; \alpha), \quad \frac{dw}{d\tau} = \epsilon g(u, w). \quad (38)$$

Unlike the case of one fast and two slow variables considered in [36], here there are two fast variables (u, v) and one slow variable (w). There is a one-dimensional “slow” manifold (on which the dynamics evolve with a timescale $1/\epsilon$) given by

$$\begin{aligned} S^{3\text{D}}(\alpha) &\equiv \{(u, v, w) \mid f_u(u, v) = f_v(u, v, w; \alpha) = 0\} \\ &\equiv \{(u, v, w) \mid (u, v, w) = (u, \tilde{v}(u), \tilde{w}(u; \alpha))\}, \end{aligned} \quad (39)$$

where $\tilde{w}(u; \alpha)$ is given by the right-hand side of (20), and

$$\tilde{v}(u) = v_s (\beta/u - \gamma - \beta u^2). \quad (40)$$

For $\epsilon = 0$, $S^{3\text{D}}$ describes a curve of fixed points for equations (9–11) with nontrivial eigenvalues shown in Figure 10 for typical parameter values; the other eigenvalue, corresponding to perturbations along $S^{3\text{D}}$, is equal to zero. It is instructive to note that the eigenvalue which remains (relatively strongly) negative over the range of u shown in Figure 10 causes trajectories to rapidly approach a two-dimensional surface. On this surface, the two cases shown in Figure 9 generically occur, with canards existing for parameter values near the transition between these cases. In the remainder of this section, we will find equations for parameter values at which canards exist by requiring the existence of a trajectory which stays within $\mathcal{O}(\epsilon)$ of $S^{3\text{D}}$.

From (38), trajectories obey

$$f_u(u, v) \frac{\partial v}{\partial u} = f_v(u, v, w; \alpha), \quad (41)$$

$$f_u(u, v) \frac{\partial w}{\partial u} = \epsilon g(u, w). \quad (42)$$

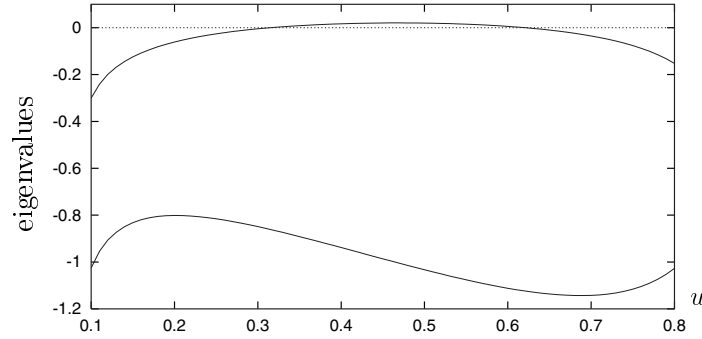


Fig. 10. Nontrivial eigenvalues as a function of u for the curve of fixed points S^{3D} for (38) with $T = 540K$, $p_{CO} = 45 \times 10^{-6}$ mbar, and $p_{O_2} = 148 \times 10^{-6}$ mbar but with ϵ artificially taken to be zero.

We expand α in powers of ϵ about a fixed value α_0^{3D} to be defined below:

$$\alpha = \alpha_0^{3D} + \epsilon \alpha_1^{3D} + \epsilon^2 \alpha_2^{3D} + \dots, \quad (43)$$

and seek an approximation to the canard manifold as a curve parametrized by u (cf. (39)):

$$\begin{aligned} v(u) &= v_0^{3D}(u) + \epsilon v_1^{3D}(u; \alpha_0^{3D}) + \epsilon^2 v_2^{3D}(u; \alpha_0^{3D}, \alpha_1^{3D}) + \dots, \\ w(u) &= w_0^{3D}(u; \alpha_0^{3D}) + \epsilon w_1^{3D}(u; \alpha_0^{3D}, \alpha_1^{3D}) + \epsilon^2 w_2^{3D}(u; \alpha_0^{3D}, \alpha_1^{3D}, \alpha_2^{3D}) + \dots. \end{aligned}$$

At $\mathcal{O}(\epsilon^0)$, equations (41,42) give

$$f_u(u, v_0^{3D}) \frac{dv_0^{3D}}{du} = f_v(u, v_0^{3D}, w_0^{3D}; \alpha_0^{3D}), \quad (44)$$

$$f_u(u, v_0^{3D}) \frac{dw_0^{3D}}{du} = 0. \quad (45)$$

For a nontrivial w_0^{3D} , (44,45) imply that

$$f_u(u, v_0^{3D}) = 0, \quad f_v(u, v_0^{3D}, w_0^{3D}; \alpha_0^{3D}) = 0. \quad (46)$$

Then,

$$v_0^{3D}(u) = \tilde{v}(u), \quad w_0^{3D}(u; \alpha_0) = \tilde{w}(u; \alpha_0) = w_0(u; \alpha_0), \quad (47)$$

where $\tilde{v}(u)$ and $w_0(u; \alpha_0)$ are given by equations (40) and (31), respectively.

To determine α_0 , we consider equations (41,42) at $\mathcal{O}(\epsilon)$ and use (46) to obtain

$$\begin{aligned} w_1^{3D}(u; \alpha_0^{3D}, \alpha_1^{3D}) &= \frac{A(u; \alpha_0^{3D})}{B(u; \alpha_0^{3D})} - \frac{\alpha_1^{3D}}{\alpha_0^{3D}} (w_0^{3D} + s), \\ v_1^{3D}(u; \alpha_0^{3D}) &= -\frac{v_s(h(u) - w_0^{3D})}{u w_0^{3D}}, \end{aligned}$$

where the prime denotes differentiation with respect to u , and

$$\begin{aligned} A(u; \alpha_0^{3D}) &= v_s(h(u) - w_0^{3D})(2\alpha_0^{3D}((u-1)v_s + v_0^{3D})(w_0^{3D} + s) + uv_s(v_0^{3D'} - 1)), \\ B(u; \alpha_0^{3D}) &= uw_0^{3D'}\alpha_0^{3D}(v_0^{3D} + (u-1)v_s)^2; \end{aligned}$$

for brevity, here $w_0^{3D} = w_0^{3D}(u; \alpha_0^{3D})$ and $v_0^{3D} = v_0^{3D}(u)$. Defining u_M^{3D} to be the u coordinate at the local minimum of the graph of $w_0^{3D}(u; \alpha_0^{3D})$ vs. u , we see that to keep v_1^{3D} bounded (as required for the asymptotic expansion to be valid), we need to choose α_0^{3D} to satisfy the simultaneous equations

$$w_0^{3D}(u_M^{3D}; \alpha_0^{3D}) = h(u_M^{3D}), \quad w_0^{3D'}(u_M^{3D}; \alpha_0^{3D}) = 0. \quad (48)$$

Recalling from (47) that $w_0^{3D} = w_0$, these equations are *identical* to (33) for the two-dimensional model. Thus,

$$\alpha_0^{3D} = \alpha_0, \quad u_M^{3D} = u_M.$$

Note that $B(u_M^{3D}; \alpha_0^{3D}) = 0$, so to keep w_1^{3D} bounded it is necessary that

$$A(u_M^{3D}, \alpha_0^{3D}) = 0,$$

a condition that holds when $w_0^{3D}(u_M^{3D}; \alpha_0^{3D}) = h(u_M^{3D})$ as in (48). As was found in the asymptotic analysis of the two-dimensional model, using (11) we conclude that the value of α_0^{3D} is that for which a fixed point to (38) exists at the ‘‘fold’’ in S^{3D} at $(u, v, w) = (u_M^{3D}, v_0^{3D}(u_M^{3D}), w_0^{3D}(u_M^{3D}; \alpha_0^{3D}))$.

At $\mathcal{O}(\epsilon^2)$, equations (42) and (46) imply that

$$v_2^{3D}(u; \alpha_0^{3D}, \alpha_1^{3D}) = \frac{v_s w_1^{3D}(u; \alpha_0^{3D}, \alpha_1^{3D}) - uv_1^{3D}(u; \alpha_0^{3D})w_1^{3D'}(u; \alpha_0^{3D}, \alpha_1^{3D})}{uw_0^{3D'}(u; \alpha_0^{3D})}.$$

The denominator of this expression vanishes at $u = u_M^{3D}$, so to keep v_2^{3D} bounded it is necessary that

$$\lim_{u \rightarrow u_M^{3D}} [v_s w_1^{3D}(u; \alpha_0^{3D}, \alpha_1^{3D}) - uv_1^{3D}(u; \alpha_0^{3D})w_1^{3D'}(u; \alpha_0^{3D}, \alpha_1^{3D})] = 0.$$

Evaluating this limit requires several applications of L'Hôpital's rule, finally giving

$$\alpha_1^{3D} = \alpha_0^{3D} \frac{A'' B' h' - A' B'' h' + 2A' B' w_0''}{2(B')^2(w_0 + s)w_0''}, \quad (49)$$

where all functions and derivatives are evaluated at $(u, \alpha) = (u_M^{3D}, \alpha_0^{3D})$. This may be solved for specific parameters using, e.g., Mathematica. Note that the requirement that w_2^{3D} remain bounded gives no further information.

As for the analysis of the two-dimensional model, we could continue this procedure to find $\alpha_2^{3D}, \alpha_3^{3D}, \dots$. However, as shown in the next section, the given calculations predict the parameter values for which canards exist with excellent accuracy.

6. Comparison of Asymptotic and Numerical Results

In this section, we compare the predictions from the asymptotic analysis given in Sections 4 and 5 with numerical results. We first consider the parameter values $T = 540K$ and $p_{CO} = 45 \times 10^{-6}$ mbar. The values of β and γ are given in (21), and

$$\epsilon = 0.000682425.$$

From (33) (and, equivalently, (48)),

$$\alpha_0 = \alpha_0^{3D} = 0.0810229, \quad u_M = u_M^{3D} = 0.314457.$$

Thus, to lowest order the predicted value of p_{O_2} for which canard manifold exists is

$$p_{O_2}^{a,0} \approx \frac{k_r v_s}{\kappa_o (s_{o1} - s_{o2})} \alpha_0 = 148.7597 \times 10^{-6} \text{ mbar}.$$

Recalling (5) and (17), we see that $p_{O_2}^{h,2D}$, $p_{O_2}^{h,3D} < p_{O_2}^{a,0}$. But we know numerically that the value of p_{O_2} at which the canard manifold exists is *smaller* than the value at which the Hopf bifurcation occurs (cf. Figure 2). We conclude that the lowest-order approximation is not very good.

To next order for the two-dimensional model, using (36) we obtain

$$\alpha_1 = -0.680652.$$

Thus, to this order the canard manifold is predicted to exist at

$$p_{O_2}^{a,2D} \approx \frac{k_r v_s}{\kappa_o (s_{o1} - s_{o2})} (\alpha_0 + \epsilon \alpha_1) = 147.9069 \times 10^{-6} \text{ mbar}.$$

Comparing this prediction with the numerically obtained values for the two-dimensional model (see (16)) and for the full three-dimensional model (see (6)), we find that

$$|p_{O_2}^{c,2D} - p_{O_2}^{a,2D}|/p_{O_2}^{c,2D} \approx 8 \times 10^{-6}, \quad |p_{O_2}^{c,3D} - p_{O_2}^{a,2D}|/p_{O_2}^{c,3D} \approx 1 \times 10^{-3} :$$

respectively only a 0.0008% and 0.1% error! It is not surprising that the prediction is better for the two-dimensional model; however, the prediction is also very good for the full three-dimensional model.

For the three-dimensional model, using (49) we obtain

$$\alpha_1^{3D} = -0.816185.$$

Thus, to this order the canard manifold is predicted to exist at

$$p_{O_2}^{a,3D} \approx \frac{k_r v_s}{\kappa_o (s_{o1} - s_{o2})} (\alpha_0^{3D} + \epsilon \alpha_1^{3D}) = 147.7371 \times 10^{-6} \text{ mbar}.$$

We find that

$$|p_{O_2}^{c,2D} - p_{O_2}^{a,3D}|/p_{O_2}^{c,2D} \approx 1 \times 10^{-3}, \quad |p_{O_2}^{c,3D} - p_{O_2}^{a,3D}|/p_{O_2}^{c,3D} \approx 3 \times 10^{-5} :$$

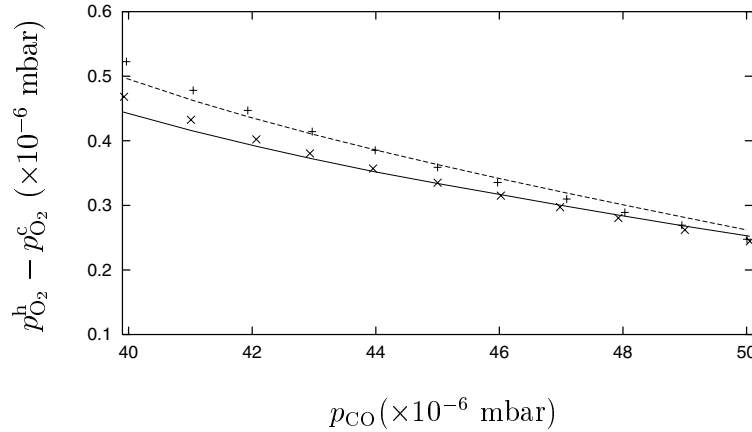


Fig. 11. Difference between the value $p_{O_2}^h$ at which the Hopf bifurcation occurs and the value $p_{O_2}^c$ at which the canard manifold exists for fixed $T = 540K$ and different values of p_{CO} . The solid (dashed) line corresponds to the asymptotic results to first order in ϵ calculated as $p_{O_2}^{h,2D} - p_{O_2}^{a,2D} (p_{O_2}^{h,3D} - p_{O_2}^{a,3D})$. The \times 's ($+$'s) show numerical results calculated as $p_{O_2}^{h,2D} - p_{O_2}^{c,2D} (p_{O_2}^{h,3D} - p_{O_2}^{c,3D})$.

respectively only a 0.1% and 0.003% error! It is not surprising that here the prediction is better for the three-dimensional model; however, the prediction is also very good for the two-dimensional model.

As a further comparison, Figure 11 shows asymptotic and numerical results for the difference between the value $p_{O_2}^h$ at which the Hopf bifurcation occurs and the value $p_{O_2}^c$ at which the canard manifold exists; note that these values are calculated for the three-dimensional model (9–11) or the two-dimensional model (13,14) as indicated by “3D” and “2D,” respectively. This may be thought of as the width of the interval over which the “small” periodic orbit exists. The asymptotic analysis shows good agreement with the numerical results for both the two-dimensional and the three-dimensional models.

7. Canards and Saddle-Loop Bifurcations

This section describes the relationship between canards and saddle-loop bifurcations associated with codimension-two Takens-Bogdanov and saddle-node loop bifurcations [45], [38]. Note that as the bifurcation set for a saddle-loop bifurcation is approached from one side, a periodic orbit approaches a saddle fixed point, and its period tends to infinity; on the other side of the bifurcation set, the periodic orbit no longer exists. The parameter values at which saddle-loop bifurcations occur can be found analytically in a small neighborhood of a Takens-Bogdanov bifurcation [45], but in general they must be found numerically. However, as we will see, here it is possible to make such predictions by considering canards. For clarity, we first consider the two-dimensional model given by (13,14), for which the codimension-two bifurcations occur at parameter values very close to those given in Table 2 for (1–3). For example, Takens-Bogdanov

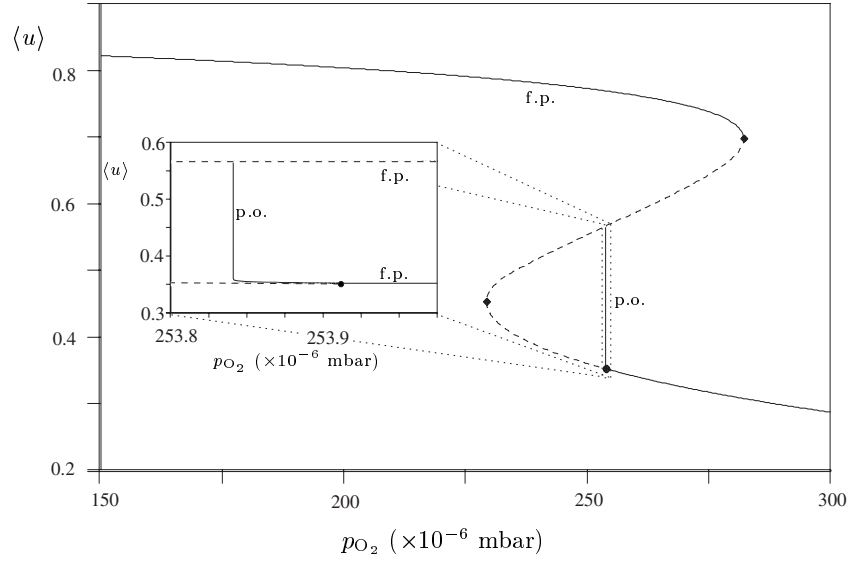


Fig. 12. Bifurcation diagram for the two-dimensional model (13,14) for fixed $T = 540K$ and fixed $p_{CO} = 60 \times 10^{-6}$ mbar with the same conventions as in Figure 2(a). The inset zooms in on the parameter range over which the periodic orbit exists. As the saddle-loop bifurcation is approached, the periodic orbit spends more time near a saddle fixed point, and $\langle u \rangle$ tends toward the u value of that fixed point.

bifurcations occur for (13,14) with $T = 540K$ at $(p_{CO}, p_{O_2}) = (32.7, 66.2) \times 10^{-6}$ mbar and $(115.0, 1295.4) \times 10^{-6}$ mbar.

Figure 12 shows a representative bifurcation diagram for the situation of interest. This is computed for the two-dimensional model (13,14) and corresponds to a slice through parameter space for fixed $T = 540K$, fixed $p_{CO} = 60 \times 10^{-6}$ mbar, and varying p_{O_2} . For decreasing p_{O_2} , a periodic orbit is born in a supercritical Hopf bifurcation and dies in a saddle-loop bifurcation at

$$p_{O_2}^{\text{h,2D}} = 253.9280 \times 10^{-6} \text{ mbar}, \quad p_{O_2}^{\text{sl,2D}} = 253.8469 \times 10^{-6} \text{ mbar},$$

respectively. Consider the phase space structure for parameters near the saddle-loop bifurcation (see Figure 13), in particular, the stable and unstable manifolds of the point P at $(u, w) \approx (0.5665, 1)$. The *unstable* manifold of P stays within $\mathcal{O}(\epsilon)$ of the line $w = 1$ until it reaches the left branch of the $\frac{du}{dt} = 0$ nullcline (cf. Figure 7); the unstable manifold then follows within $\mathcal{O}(\epsilon)$ of the nullcline until reaching the local minimum of the graph of the nullcline, labelled M . On the other hand, the *stable* manifold of P stays within $\mathcal{O}(\epsilon)$ of the middle branch of the $\frac{du}{dt} = 0$ nullcline until reaching M . A saddle-loop bifurcation occurs when these stable and unstable manifolds of P connect smoothly, which is precisely when the canard manifold exists. Thus, the asymptotic analysis given above can be used to predict parameter values at which the saddle-loop bifurcation occurs. Calculating α to $\mathcal{O}(\epsilon)$ for these parameters as in Section 4, we predict

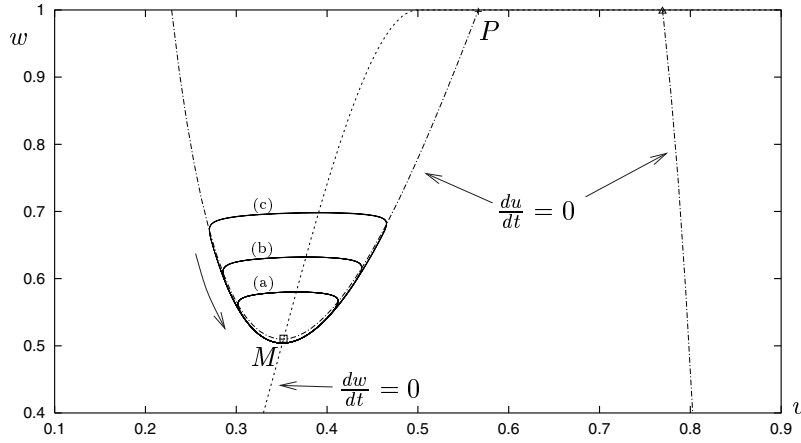


Fig. 13. Stable periodic orbits for (13,14) with $T = 540K$, $p_{CO} = 60 \times 10^{-6}$ mbar, and (a) $p_{O_2} = 253.847 \times 10^{-6}$ mbar, (b) $p_{O_2} = 253.846867 \times 10^{-6}$ mbar, and (c) $p_{O_2} = 253.846866931597 \times 10^{-6}$ mbar. The dashed line is the nullcline of $g(u, w)$, while the dash-dotted line is the nullcline of $f(u, w)$ (the nullclines do not change appreciably over the range of p_{O_2} shown in the figure). The intersections of the nullclines give fixed points, namely one source and one sink shown as a square symbol and a triangular symbol, respectively, and a saddle shown as a + and labelled P . For smaller values of p_{O_2} (even for $p_{O_2} = 253.846866931596 \times 10^{-6}$ mbar), periodic orbits no longer exist and the trajectory tends to the sink fixed point.

that the saddle-loop bifurcation occurs at

$$p_{O_2}^{sl,2D,a} = 253.8337 \times 10^{-6} \text{ mbar.}$$

Note that the corresponding Hopf and saddle-loop bifurcations for the three-dimensional model occur at

$$p_{O_2}^{h,3D} = 253.7573 \times 10^{-6} \text{ mbar,} \quad p_{O_2}^{sl,3D} = 253.7127 \times 10^{-6} \text{ mbar,}$$

respectively. Calculating α to $\mathcal{O}(\epsilon)$ as in Section 5, we predict that the saddle-loop bifurcation for the three-dimensional model occurs at

$$p_{O_2}^{sl,3D,a} = 253.6920 \times 10^{-6} \text{ mbar.}$$

Using

$$\begin{aligned} |p_{O_2}^{sl,2D} - p_{O_2}^{sl,2D,a}|/p_{O_2}^{sl,2D} &\approx 5 \times 10^{-5}, \\ |p_{O_2}^{sl,3D} - p_{O_2}^{sl,3D,a}|/p_{O_2}^{sl,3D} &\approx 6 \times 10^{-4}, \end{aligned}$$

we see that the prediction for the parameter value at which a saddle-loop bifurcation occurs for the two-dimensional and three-dimensional models have only a 0.005% and a 0.06% error, respectively.

8. Conclusion

Canards are periodic orbits for which the trajectory follows both the attracting and repelling parts of a slow manifold. They are associated with a dramatic change in the amplitude and period of a periodic orbit within a very narrow interval of a control parameter. In this paper, canards were studied both numerically and analytically for the model of platinum-catalyzed oxidation of carbon monoxide introduced in [38]. The model is a three-dimensional system of ODEs for the evolution of the surface coverage of CO, the surface coverage of oxygen, and the fraction of the surface area of Pt exhibiting a particular structure. Numerical arguments were given to justify the adiabatic approximation for the surface coverage of O₂; this reduces the three-dimensional model to a two-dimensional model in which the surface coverage of CO evolves on a fast timescale relative to the evolution of the structure of the surface (cf. [39]). This two-dimensional model was then analyzed asymptotically in the spirit of [10] to predict parameter values at which canards exist. Then, these asymptotic techniques were extended to predict parameter values at which canards exist for the full three-dimensional model. Finally, the relationship between canards and saddle-loop bifurcations for these models was described. Throughout, excellent agreement was found between the numerical and analytical results.

The three-dimensional model introduced in [38] has been extended in several ways. By also modeling the faceting of the Pt surface (that is, the formation of new crystal planes on Pt(110)), [38] was able to account for experimentally observed mixed-mode oscillations. Specifically, they introduce a new variable z for the degree of faceting, which obeys the equation

$$\frac{dz}{dt} = k_f uvw(1 - z) - k_t z(1 - u), \quad (50)$$

where the rate of facet formation is $k_f = 0.03 \text{ s}^{-1}$, and the rate of thermal annealing is $k_t = k_t^0 \exp[-E_t/(RT)]$ with $k_t^0 = 2.65 \times 10^5 \text{ s}^{-1}$ and $E_t = 20 \text{ kcal/mol}$. The increase of oxygen sticking probability due to faceting is accounted for by generalizing (4) to

$$s_o = w s_{o1} + (1 - w) s_{o2} + s_{o3} z, \quad (51)$$

where $s_{o3} = 0.2$. A stable periodic solution for equations (1–3) and (50) is shown in Figure 14. This may be interpreted (cf. [38]) by first thinking of z as a constant parameter, and noticing that for large (small) values of z a “small” (“large”) stable periodic orbit exists in the (u, v, w) variables; the intermediate periodic orbits are canards related to those described in this paper. When z is allowed to vary, it is found that z slowly decreases (increases) for a “small” (“large”) oscillation in the (u, v, w) variables. Thus, z slowly drifts back and forth, and mixed-mode oscillations occur (cf. [23]). We conclude that although the canards themselves are expected to be quite delicate and hence difficult to find experimentally, their presence can perhaps be inferred from the phenomenon of mixed-mode oscillations. A more detailed analysis of such mixed-mode oscillations is deferred to future work.

To explain the spatiotemporal patterns observed in experiments, the three-dimensional model of [38] was extended to include surface diffusion of adsorbed CO [39], [51]–[53],

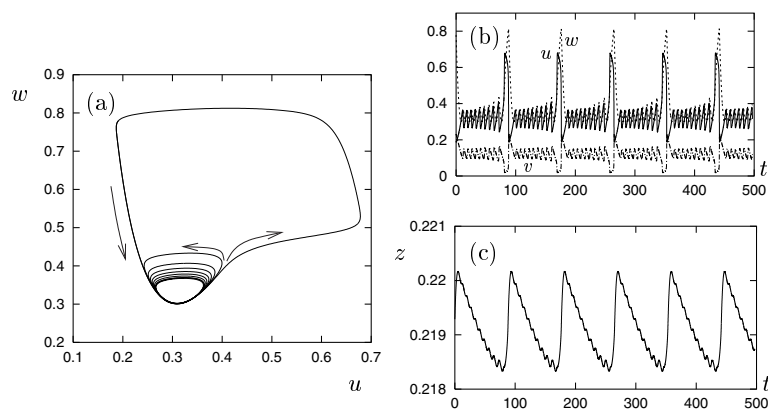


Fig. 14. Stable, periodic mixed-mode oscillations for the four-dimensional set of equations given by (1–3) and (50) for $p_{\text{CO}} = 42 \times 10^{-6}$ mbar, $p_{\text{O}_2} = 119.1 \times 10^{-6}$ mbar, and $T = 540\text{K}$. (a) The projection of the trajectory onto the (u, w) plane. (b) Time series for u , v , and w given by solid, dash-dotted, and dashed lines, respectively. (c) Time series for the faceting variable z .

giving solutions such as traveling and spiral waves. Naturally, this raises the question of how canards would be affected by diffusion (cf. [34]). More recently, the three-dimensional model with surface diffusion has been extended to include the formation and release of subsurface oxygen [54]–[56]; in the absence of surface diffusion, it is very likely that canards related to those discussed in this paper will be present for this extension. Indeed, canards are present in a large variety of systems of physical and biological interest, and the procedure presented in this paper could be used to predict parameter values at which canards exist for such systems.

Acknowledgments

This work was supported by a National Science Foundation Mathematical Sciences Postdoctoral Research Fellowship and NSF grant DMS-9803752. I would like to thank Philip Holmes and Yannis Kevrekidis for useful comments and discussions, and the referees for useful suggestions.

References

- [1] J.-L. Callot, F. Diener, and M. Diener. Le problème de la “chasse au canard,” *C. R. Acad. Sci. Paris (Sér. I)* **286**, 1059–1061, 1978.
- [2] E. Benoit, J.-L. Callot, F. Diener, and M. Diener. Chasse au canard. *Collect. Math.* **32**, 37–119, 1981.
- [3] M. Diener. The canard unchained *or* how fast/slow dynamical systems bifurcate. *Math. Intell.* **6**, 38–49, 1984.

- [4] A. K. Zvonkin and M. A. Shubin. Non-standard analysis and singular perturbations of ordinary differential equations. *Russ. Math. Surv.* **39**, 69–131, 1984.
- [5] W. Eckhaus. Relaxation oscillations including a standard chase on French ducks. *Lecture Notes in Math.* **985**, 449–494, 1983.
- [6] J. Grasman. *Asymptotic Methods for Relaxation Oscillations and Applications*. Springer-Verlag, New York, 1987.
- [7] E. F. Mishchenko, Yu. S. Kolesov, A. Yu. Kolesov, and N. Kh. Rozov. *Asymptotic methods in singularly perturbed systems*. Consultants Bureau, New York and London, 1994.
- [8] C. Kaas Peterson and M. Brøns. A computational method for the canard-explosion. In *Proceedings of the 11th IMACS World Congress on System Simulation and Scientific Computation, Vol. 4*, ed. B. Wahlstrom. North-Holland, Amsterdam, 285–287, 1985.
- [9] M. Brøns. Canards and excitability of Liénard equations. Mat-report 1989-22, Mathematical Institute, The Technical University of Denmark, 1989.
- [10] M. Brøns and K. Bar-Eli. Canard explosion and excitation in a model of the Belousov-Zhabotinsky reaction. *J. Phys. Chem.* **95**, 8706–8713, 1991.
- [11] F. Dumortier and R. Roussarie. Canard cycles and center manifolds. *Mem. Am. Math. Soc.* **121**, 1996.
- [12] M. Krupa and P. Szmolyan. Extending geometric singular perturbation theory to nonhyperbolic points—Fold and canard points in two dimensions. *SIAM J. Math. Anal.* **33**, 286–314, 2001.
- [13] M. Krupa and P. Szmolyan. Relaxation oscillation and canard explosion. *J. Diff. Eq.* **174**, 312–368, 2001.
- [14] S. M. Baer and T. Erneux. Singular Hopf bifurcation to relaxation oscillations. *SIAM J. Appl. Math.* **46**, 721–739, 1986.
- [15] S. M. Baer and T. Erneux. Singular Hopf bifurcation to relaxation oscillations II. *SIAM J. Appl. Math.* **52**, 1651–1664, 1992.
- [16] B. Braaksma. Singular Hopf bifurcation in systems with fast and slow variables. *J. Nonlinear Sci.* **8**, 457–490, 1998.
- [17] B. Braaksma. Phantom ducks and models of excitability. *J. Dyn. Diff. Eq.* **4**, 485–513, 1992.
- [18] E. Freire, E. Gamero, and A. J. Rodríguez-Luis. First-order approximation for canard periodic orbits in a van der Pol electronic oscillator. *Appl. Math. Lett.* **12**, 73–78, 1999.
- [19] V. Gáspár and K. Showalter. A simple model for the oscillatory iodate oxidation of sulfite and ferrocyanide. *J. Phys. Chem.* **94**, 4973–4979, 1990.
- [20] B. Peng, V. Gáspár, and K. Showalter. False bifurcations in chemical systems: Canards. *Phil. Trans. R. Soc. Lond. A* **337**, 275–289, 1991.
- [21] M. Brøns and K. Bar-Eli. Asymptotic analysis of canards in the EOE equations and the role of the inflection line. *Proc. R. Soc. Lond. A* **445**, 305–322, 1994.
- [22] M. Mazzotti, M. Morbidelli, and G. Serravalle. Bifurcation analysis of the Oregonator model in the 3-D space bromate/malonic acid/stoichiometric coefficient. *J. Phys. Chem.* **99**, 4501–4511, 1995.
- [23] A. Milik, P. Szmolyan, H. Löffelmann, and E. Gröller. Geometry of mixed-mode oscillations in the 3-D autocatalator. *Int. J. Bif. Chaos* **8**, 505–519, 1998.
- [24] M. Brøns and J. Sturis. Explosion of limit cycles and chaotic waves in a simple nonlinear chemical system. *Phys. Rev. E* **64**, 026209, 2001.
- [25] M. Brøns. Excitation and annihilation in the FitzHugh-Nagumo equations. *IMACS Trans. Sci. Comp.* **1.1**, 297–301, 1989.
- [26] N. Kakiuchi, K. Tchizawa. On an explicit duck solution and delay in the Fitzhugh-Nagumo equation. *J. Diff. Eq.* **141**, 327–339, 1997.
- [27] K. Gedalin. Electro-osmotic oscillations. *Physica D* **110**, 154–168, 1997.
- [28] J. Guckenheimer, K. Hoffman, and W. Weckesser. Numerical computation of canards. *Int. J. Bif. Chaos* **10**, 2669–2687, 2000.
- [29] M. Brøns. Bifurcations and instabilities in the Greitzer model for compressor system surge. *Math. Eng. Ind.* **2**, 51–63, 1988.
- [30] G. N. Gorelov and V. A. Sobolev. Duck-trajectories in a thermal explosion problem. *Appl. Math. Lett.* **5**(6), 3–6, 1992.

- [31] V. A. Sobolev and E. A. Shchepakina. Duck trajectories in a problem of combustion theory. *Diff. Eq.* **32**, 1177–1186, 1996.
- [32] J. Guckenheimer and Yu. Ilyashenko. The duck and the devil: Canards on the staircase. *Moscow Math. J.* **1**, 27–47, 2001.
- [33] E. Shchepakina and V. Sobolev. Integral manifolds, canards and black swans. *Nonlinear Anal.* **44**, 897–908, 2001.
- [34] F. Buchholtz, M. Dolnik, and I. R. Epstein. Diffusion-induced instabilities near a canard. *J. Phys. Chem.* **99**, 15093–15101, 1995.
- [35] V. I. Arnold, V. S. Afrajmovich, Yu. S. Il'yashenko, and L. P. Shil'nikov. *Dynamical Systems V*, Encyclopaedia of Mathematical Sciences, Springer-Verlag, 1994.
- [36] P. Szmolyan and M. Wechselberger. Canards in \mathbb{R}^3 . *J. Diff. Eq.* **177**, 419–453, 2001.
- [37] J. Guckenheimer and B. Meloon. Computing periodic orbits and their bifurcations with automatic differentiation. *SIAM J. Sci. Comput.* **22**, 951–985, 2000.
- [38] K. Krischer, M. Eiswirth, and G. Ertl. Oscillatory CO oxidation on Pt(110): Modeling of temporal self-organization. *J. Chem. Phys.* **96**, 9161–9172, 1992.
- [39] M. Falcke, M. Bär, H. Engel, and M. Eiswirth. Traveling waves in the CO oxidation on Pt(110): Theory. *J. Chem. Phys.* **97**, 4555–4563, 1992.
- [40] M. M. Slin'ko and N. I. Jaeger. *Oscillating Heterogeneous Catalytic Systems*. Elsevier, Amsterdam, 1994.
- [41] T. Engel and G. Ertl. Elementary steps in the catalytic oxidation of carbon monoxide on platinum metals. *Adv. Catal.* **28**, 1–78, 1979.
- [42] G. Ertl. Oscillatory catalytic reactions at single-crystal surfaces. *Adv. Catal.* **37**, 213–277, 1990.
- [43] E. Doedel, A. Champneys, T. Fairgrieve, Y. Kuznetsov, B. Sandstede, and X. Wang. AUTO 97: Continuation and bifurcation software for ordinary differential equations. Available via FTP from directory pub/doedel/auto at ftp.cs.concordia.ca, 1997.
- [44] J. Kevorkian and J. D. Cole. *Multiple Scale and Singular Perturbation Methods*. Springer-Verlag, New York, 1996.
- [45] J. Guckenheimer and P. Holmes. *Nonlinear Oscillations, Dynamical Systems, and Bifurcations of Vector Fields*. Springer-Verlag, New York, 1983.
- [46] N. Fenichel. Persistence and smoothness of invariant manifolds for flows. *Indiana Univ. Math. J.* **21**, 193–226, 1971.
- [47] N. Fenichel. Geometric singular perturbation theory for ordinary differential equations. *J. Diff. Eq.* **31**, 53–98, 1979.
- [48] S. Wiggins. *Normally Hyperbolic Invariant Manifolds in Dynamical Systems*. Springer-Verlag, New York, 1994.
- [49] J. Carr. *Applications of Center Manifold Theory*. Springer-Verlag, New York, 1981.
- [50] M. Canalis-Durand. Formal expansion of van der Pol equation canard solutions are Gevrey. *Lecture Notes in Math.* **1493**, 29–39, 1991.
- [51] M. Bär, M. Falcke, C. Zülicke, H. Engel, M. Eiswirth, and G. Ertl. Reaction fronts and pulses in the CO oxidation on Pt—Theoretical analysis. *Surf. Sci.* **270**, 471–475, 1992.
- [52] M. Bär, M. Eiswirth, H.-H. Rotermund, and G. Ertl. Solitary-wave phenomena in an excitable surface reaction. *Phys. Rev. Lett.* **69**, 945–948, 1992.
- [53] M. Bär, N. Gottschalk, M. Eiswirth, and G. Ertl. Spiral waves in a surface reaction: Model calculations. *J. Chem. Phys.* **100**, 1202–1214, 1994.
- [54] A. von Oertzen, A. Mikhailov, H.-H. Rotermund, and G. Ertl. Subsurface oxygen formation on the Pt(110) surface: Experiment and mathematical modeling. *Surf. Sci.* **350**, 259–270, 1996.
- [55] A. von Oertzen, A. S. Mikhailov, H.-H. Rotermund, and G. Ertl. Subsurface oxygen in the CO oxidation reaction on Pt(110): Experiments and modeling of pattern formation. *J. Phys. Chem. B* **102**, 4966–4981, 1998.
- [56] A. von Oertzen, H.-H. Rotermund, A. S. Mikhailov, and G. Ertl. Standing wave patterns in the CO oxidation reaction on a Pt(110) surface: Experiments and modeling. *J. Phys. Chem. B* **104**, 3155–3178, 2000.